

Improved Diffusion Tensor Imaging of the Optic Nerve Using Multishot Two-Dimensional Navigated Acquisitions

Ha-Kyu Jeong,^{1,2} Blake E. Dewey,^{3,4} Jane A.T. Hirtle,^{3,5} Patrick Lavin,^{6,7} Subramaniam Sriram,⁶ Siddharama Pawate,⁶ John C. Gore,^{3,4,8,9} Adam W. Anderson,^{3,4,8,9} Hakmook Kang,¹⁰ and Seth A. Smith^{3,4,8,9*}

Purpose: A diffusion-weighted multishot echo-planar imaging approach combined with SENSE and a two-dimensional (2D) navigated motion correction was investigated as an alternative to conventional single-shot counterpart to obtain optic nerve images at higher spatial resolution with reduced artifacts.

Methods: Fifteen healthy subjects were enrolled in the study. Six of these subjects underwent a repeated acquisition at least 2 weeks after the initial scan session to address reproducibility. Both single-shot and multishot diffusion tensor imaging studies of the human optic nerve were performed with matched scan time. Effect of subject motions were corrected using 2D phase navigator during multishot image reconstruction. Tensor-derived indices from proposed multishot were compared against conventional single-shot approach. Image resolution difference, right–left optic nerve asymmetry, and test–retest reproducibility were also assessed.

Results: In vivo results of acquired multishot images and quantitative maps of diffusion properties of the optic nerve showed significantly reduced image artifacts (e.g., distortions and blurring), and the derived diffusion indices were comparable to those from other studies. Single-shot scans presented larger variability between right and left optic nerves than multishot scans. Multishot scans also presented smaller variations across scans at different time points when compared with single-shot counterparts.

Conclusion: The multishot technique has considerable potential for providing improved information on optic nerve pathology and may also be translated to higher fields.

Magn Reson Med 74:953–963, 2015. © 2014 Wiley Periodicals, Inc.

Key words: optic nerve; DTI; multishot; 2D navigator

INTRODUCTION

The human optic nerve is a small (<3 mm) white matter bundle that exits the globe and courses posteriorly to the optic chiasm; it sits inside layers of cerebrospinal fluid, meninges, fat, muscle, and bone and is proximal to four large sinuses. Among others, a prevalent condition affecting the optic nerve is optic neuritis, an acute inflammation of the optic nerve that has been implicated in the development of multiple sclerosis (1). Importantly, small lesions in the optic nerve may result in blurred vision, decreased visual acuity, decreased color vision, and central and segmental scotomas, which can be transient or permanent. Radiologically, abnormal MRI appearance of the optic nerves is not always specific for demyelination or axonal loss (2,3) and may not always correlate with the degree of visual dysfunction or permanence of disability. Therefore, attention has turned to developing quantitative methods such as magnetization transfer (4–7) and diffusion-weighted imaging (8–21). Diffusion-weighted imaging has been used to study the optic nerve, partly because of its increased specificity over conventional MRI (22,23). For example, diffusion anisotropy derived from diffusion tensor imaging (DTI) can reveal microstructural detail of white matter fibers. Although diffusion MRI has largely been limited to the brain (23–25), the optic nerve is a pure white matter structure that is well suited for evaluation by diffusion MRI and may provide novel information about optic neuritis and diseases such as multiple sclerosis (11). Recent studies have reported correlations between the calculated indices of diffusion and visual function (e.g., high/low contrast visual acuity) (14,15,26) and optical coherence tomography measures (e.g., retinal nerve fiber layer thickness) (15,27).

A limitation of optic nerve diffusion-weighted (DW) MRI is the utilization of single-shot (ssh) echo-planar imaging (EPI) sequences. Although ssh-EPI readouts can generate images within a fraction of a second and are relatively insensitive to subject motion (28), they can often lead to significant artifacts such as geometric distortions, signal losses, and blurring. These are especially severe in regions of large susceptibility variations (e.g., near the

¹Philips Healthcare Korea, Seoul, Republic of Korea.

²Division of Magnetic Resonance Research, Korea Basic Science Institute, Chungbook, Republic of Korea.

³Vanderbilt University Institute of Imaging Science, Vanderbilt University, Nashville, Tennessee, USA.

⁴Department of Physics and Astronomy, Vanderbilt University, Nashville, Tennessee, USA.

⁵Department of Psychology and Human Development, Vanderbilt University, Nashville, Tennessee, USA.

⁶Department of Neurology, Vanderbilt University, Nashville, Tennessee, USA.

⁷Department of Ophthalmology, Vanderbilt University, Nashville, Tennessee, USA.

⁸Department of Radiology and Radiological Sciences, Vanderbilt University, Nashville, Tennessee, USA.

⁹Department of Biomedical Engineering, Vanderbilt University, Nashville, Tennessee, USA.

¹⁰Department of Biostatistics, Vanderbilt University, Nashville, Tennessee, USA.

Grant sponsor: National Institutes of Health; Grant number: R01-EB000461; Grant sponsor: National Institute of Biomedical Imaging and Bioengineering; Grant number: K01-EB0009120.

*Correspondence to: Seth A. Smith, Ph.D., Vanderbilt University Institute of Imaging Science, 1161 21st Avenue South, Medical Center North, AA-1105, Nashville, TN 37232-2310. E-mail: seth.smith@vanderbilt.edu

Received 17 March 2014; revised 8 August 2014; accepted 29 August 2014

DOI 10.1002/mrm.25469

Published online 26 September 2014 in Wiley Online Library (wileyonlinelibrary.com).

© 2014 Wiley Periodicals, Inc.

Table 1
Other Imaging Parameters Specific to Acquisition Methods

Method	Voxel size (mm ³) ^a	TR/TE (ms) ^b	N_{avg}	N_{shot}	Scan time (min:s)
ssh	$1.5 \times 1.5 \times 3$	2359/38	10	1	7:09
msh	$1.5 \times 1.5 \times 3$	1932/(64, 93)	8	2	7:22
	$1.25 \times 1.25 \times 3$	1947/(67, 98)	5	3	7:29
	$1.25 \times 1.25 \times 2$	2073/(66, 97)	5	3	7:47

^aReadout \times phase-encoding \times slice.

^bFor msh, the TR/TE values are presented as TR/TE (image-echo, navigator-echo).

sinuses). Most problematic, however, is that high spatial resolution is desirable for optic nerve assessment, which, in ssh-EPI, requires longer echo-trains that exacerbate image artifacts and increased number of acquisitions to provide reasonable signal-to-noise ratio (SNR). One approach to improve resolution and SNR is to employ higher B_0 field strengths, but artifacts arising from susceptibility variations scale with B_0 . Consequently, conventional ssh-EPI struggles to produce DTI data of sufficiently high quality and spatial resolution for assessment of the human optic nerve in vivo. Alternate methods have challenged these limitations, including CO-ZOOM (contiguous-slice zonally oblique multislice) (9) and reduced field of view (12,14,21) acquisitions, which reduce the number of phase-encoding lines and thus the overall echo train length. Sensitivity encoding (SENSE) (29) and the use of B_0 field maps have also been used to reduce geometric distortions (17). Cardiac gating has been used to suppress pulsatile brain motion and has been applied to the optic nerve (13,21). Other pulse sequences such as spin-echo (11) and non-Carr-Purcell-Meiboom-Gill fast spin-echo have been suggested for reducing susceptibility-induced artifacts (8). Unwanted cerebrospinal fluid (CSF) and fat signals also may be suppressed to reduce artifacts such as an inversion recovery preparation (9,10,17,19,20) for CSF suppression or spectral-spatial excitation pulses (10,19,20), spectral presaturation with inversion recovery (SPIR) (17), or slice-selective gradient reversal techniques (21) for fat reduction. Outer volume suppression techniques have also been used to minimize signals other than the optic nerve and surrounding regions (8). It should be pointed out, however, that some of these advanced methods may still suffer from reduced SNR, residual EPI distortions and blurring, high specific absorption rate, limited slice coverage and relatively long acquisition time.

We propose a different approach to mitigate some of the adverse effects of single-shot methods, which is to use a multishot (msh) EPI readout for DW acquisitions, which reduces the echo-train length and provides the opportunity for higher SNR and spatial resolution. However, msh-EPI, when combined with diffusion weighting, suffers from phase inconsistencies caused by bulk tissue motion between shots (30,31). The phase inconsistency generates severe ghosting in the reconstructed DW images unless it is properly compensated. To this end, one-dimensional navigator-echo corrections have been employed successfully (30,31). Higher dimension corrections, both two-dimensional (2D) (32–38) and three-dimensional (39,40), are used primarily for brain studies. We investigated a DW msh-EPI approach combined with parallel imaging (SENSE) and a 2D navigator as an alternative to ssh-EPI DW acquisitions to obtain DW images at higher spatial

resolution, with reduced artifacts, for the human optic nerve (41). The use of an msh-DTI approach for optic nerve imaging has been suggested (15,42), but, to the best of our knowledge, this is the first published study to utilize msh-EPI with parallel imaging and 2D-navigated DW motion correction strategy to provide high resolution, reproducible DTI-derived indices for the human optic nerve in vivo.

METHODS

Data Acquisition

This study was approved by the local Institutional Review Board, and signed informed consent was obtained from all of the participants. Fifteen healthy subjects (male, $n = 6$; female, $n = 9$; mean age, 29.6 ± 13.9 y) were enrolled. Six subjects also underwent a repeated acquisition at least 2 weeks after the initial scan to address reproducibility. All acquisitions were obtained with a 3T Philips Achieva MRI scanner (Philips Healthcare, Best, The Netherlands) using a body coil for transmission and an eight-channel SENSE head coil for reception. All scans were performed without ocular fixation. Fast, T2-weighted turbo spin-echo acquisitions were obtained in coronal, transverse, and sagittal orientations (<1 min each) to optimally view the course of the optic nerves. The anatomical images were utilized to set optimal slice position and angulation for all DW imaging scans. Short (~1 min) msh DW images were acquired with one non-DW and one DW image to verify appropriate fat suppression, shimming, and visualization of the optic nerve. msh-DTI and ssh-DTI images were then acquired using the following imaging parameters: field of view 100×100 mm²; SENSE factor $R = 2$; 12 oblique coronal slices; diffusion-weighting b -value = 500 s/mm²; and 15 non-coplanar diffusion-encoding gradient orientations. Partial Fourier acquisition was implemented in all ssh-DTI acquisitions (factor = 0.7) to further reduce echo-train length (13 for msh-DTI, 35 for ssh-DTI). Other imaging parameters, including nominal resolution, pulse repetition time (TR)/echo time (TE) for image and navigator echoes, number of acquisitions averaged (N_{avg}), number of shots (N_{shot}), and scan time, are given in Table 1. Note that ssh-DTI 1.25×3 (in-plane \times slice thickness) mm³ data were not used for analyses due to significant image distortions and blurring. ssh-DTI and msh-DTI images were interpolated to achieve a reconstructed in-plane resolution of 0.39 mm². Because msh-DTI acquisitions require longer scan times than ssh-EPI acquisitions, we chose to match the scan time rather than the N_{avg} . Therefore, all DTI acquisitions were obtained in similar scan times of about 8 min (Table 1). To remove signals from the lateral aspect of the field of

view, outer volume suppression was used and orbital fat was suppressed using frequency-selective prepulse (SPIR) before every excitation pulse. Separate coil reference scans and static field maps were acquired (< 2 min each) for off-line msh-DTI image reconstruction (41).

For msh-DTI acquisitions, a DW msh dual spin-echo EPI pulse sequence was used as described by Jeong et al. (41). Both the image-echo and navigator-echo acquisitions were SENSE accelerated, but the image-echo k -space traversal was further accelerated using interleaved msh-EPI providing actual k -space undersampling per shot as $N_{\text{shot}} \times R$. Combining parallel imaging and msh-EPI readouts, the acquisition bandwidth per voxel and echo-train per shot were improved while the effects of eddy currents, blurring, and susceptibility-induced image distortions were minimized. After a second refocusing pulse, a pre-phasing gradient was used with constant amplitude to acquire the same segment of navigator-echo k -space for every shot as described by Jeong et al. (41). For smooth k -space magnitude and phase modulations, echo time shifting was applied (43,44). All msh-DTI images were reconstructed using the approach described by Jeong et al. (41).

Data Analysis

From the reconstructed DW images, the diffusion tensor was estimated and the parallel (λ_{\parallel}), perpendicular (λ_{\perp}), and mean diffusivity (MD), and fractional anisotropy (FA) were calculated. The calculation of the diffusion tensor and estimates of the DTI-derived indices were performed in MATLAB (MathWorks, Natick, Massachusetts, USA) using the standard formalism (22,45). For region of interest (ROI) placement, the MD, FA, and non-DW images were viewed side by side by a trained rater (B.E.D.). Similar to the study by Smith et al. (15), ROIs were drawn in MIPAV (National Institutes of Health, Bethesda, Maryland, USA) on the MD image for each eye and slice along intraorbital optic nerve segment where the nerve was clearly visible (46). The MD was chosen as described by Smith et al. (15) because the calculated indices revealed that it possessed the maximal visual contrast between CSF and the optic nerve. Each ROI was then exported to MATLAB for further statistical analyses.

Statistical Analysis

Because the number of voxels per ROI, the slices, and the subjects may vary, we performed statistical evaluation using two methods. First, we calculated the weighted average and standard deviation of each DTI-derived index using the equation

$$\begin{aligned} \text{Mean} &= \sum_{i,j} w_{ij} x_{ij} = \bar{X} \\ \text{SD} &= \sqrt{\sum_{i,j} w_{ij} (\bar{X} - x_{ij})^2}, \\ w_{ij} &= \frac{n_{ij}}{N}, \sum_{i,j} w_{ij} = 1 \end{aligned} \quad [1]$$

where the indices i and j are for the i^{th} slice and j^{th} subject, w is the weighting factor (proportion of the total voxel number), N is the total number of voxels (across all slices and subjects) in the cohort examined, n is the

number of voxels, and \bar{X} is the mean value across all slices and subjects for each acquisition. Because this approach does not capture the potential for nested variance structures or asymmetric number of voxels between eyes and may potentially underestimate the variance, we also computed the mean absolute difference (MAD) of all possible left and right optic nerve voxel pairs drawn from an empirically determined distribution (below). If there are n voxels in the right and m voxels in the left optic nerve for a single subject, then the MAD is given by

$$\text{MAD} = \left(\frac{1}{mn} \right) \sum_{k=1}^m \sum_{l=1}^n |h_k(\text{Left}) - h_l(\text{Right})|, \quad [2]$$

where $h_k(\text{Left})$ denotes a measure (e.g., FA) on the k^{th} voxel in the left optic nerve and similarly, $h_l(\text{Right})$ denotes the same measure (e.g., FA) on the l^{th} voxel of the right optic nerve. The distribution of data for each DTI index was empirically constructed via the bootstrap method with 3000 iterations. For each iteration, the subject-level DTI index data were resampled with replacement, and the empirical 95% confidence interval of the MAD for each index of interest was computed and examined for statistical significance. Therefore, for each technique (ssh versus msh), a single MAD was computed and the difference in MAD between techniques was assessed using a Wilcoxon signed-rank test. Analyses involving multiple statistical comparisons were corrected using a false discovery rate threshold of 0.05.

We compared the msh-DTI to ssh-DTI in three ways: 1) evidence for asymmetry between right and left optic nerves using both weighted and MAD analyses, 2) significant differences of msh-DTI-derived indices across resolutions using weighted analyses exclusively, and 3) reproducibility of the diffusion-derived metrics of interest using weighted and MAD analyses.

Cross-sectional Analysis

Each DTI-derived index of each acquisition scheme was evaluated for differences between eyes (assuming both eyes in healthy subjects should be statistically equivalent). An unpaired t test [accounting for weighting (47)] was used to determine whether the mean (over slices and subjects) quantity of interest derived from the right and left optic nerves were statistically equivalent. Additionally, to strictly compare msh-DTI and ssh-DTI at the same resolutions ($1.5 \times 1.5 \times 3$ mm³), we studied differences in the MAD for each index of interest. We assumed in healthy subjects that no differences should exist for each DTI-derived index between the left and right optic nerves and that a low MAD indicates a greater symmetry between the right and left optic nerves for a given DTI index and acquisition strategy (msh versus ssh). Comparing across techniques (msh-DTI and ssh-DTI), we calculated the $\Delta\text{MAD}\%$ as the difference in the MAD values for each technique relative to the MAD for the ssh-DTI acquisition as in the following equation:

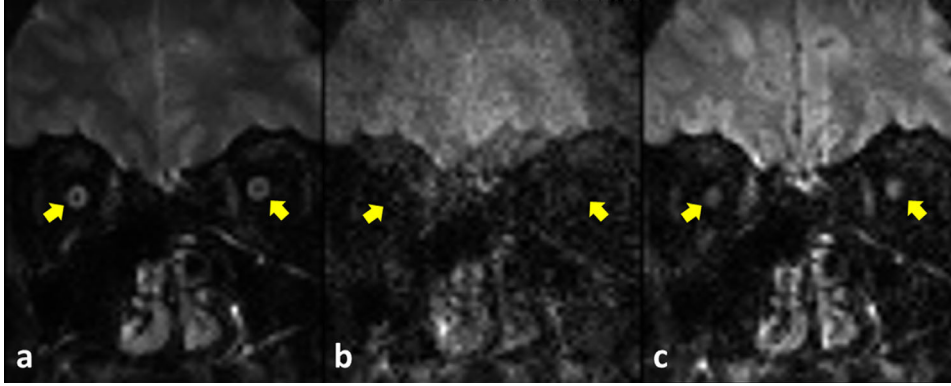


FIG. 1. Multishot images ($1.25 \times 3 \text{ mm}^3$) of non-DW (a) and 500 s/mm^2 (b,c) acquisitions before (b) and after (c) motion-induced phase correction using 2D navigation. Images without (b) and with (c) correction were reconstructed using the same number of signal acquisitions. The positions near the subject's left and right optic nerves are marked with right and left yellow arrows, respectively.

$$\Delta MAD\% = \frac{MAD(msh) - MAD(ssh)}{MAD(ssh)} \times 100. \quad [3]$$

A negative $\Delta MAD\%$ indicates a lower MAD (msh-DTI) compared with MAD (ssh-DTI), and the $\Delta MAD\%$ is an estimate of the relative improvement (or worsening) of our msh-DTI relative to the gold standard ssh-DTI. The 95% confidence interval for the MAD from each technique was calculated, and an overlap indicated no evidence for statistically significant differences (at the $\alpha = 0.05$ level) in the right-left optic nerve symmetry across techniques for each DTI-derived index.

We also compared the msh-DTI-derived indices across resolutions to determine whether resolution plays a role in the consistency of the derived index of interest. Thus, to compare across resolutions using only msh-DTI, the weighted mean index value for each eye from each participant was entered into a weighted t test. A significance threshold of $\alpha = 0.05$ was imposed.

Test-Retest Reproducibility

For each optic nerve, the DTI-derived indices from each of two time points were compared in three ways. Prior to statistical analysis, the weighted mean (over slices) value for each metric was calculated for each subject ($n = 6$) and each visit. First, Bland-Altman (48) analysis was performed to calculate whether the differences between the two time points were significantly different from 0 (i.e., if the 95% confidence interval of the difference between two raters did not encompass 0) for each MRI quantity as well as the limits of agreement, which can be used to assess whether a particular difference is outside the expected range. It should be noted that each subject contributed one value to the Bland-Altman analysis per time point, the weighted mean value of the DTI-derived index of interest, where the weighted mean was calculated across both eyes and all slices where the optic nerve was visible. Second, a Wilcoxon signed-rank test ($\alpha = 0.05$) was performed to determine whether there was an observable difference in the median values between the two time points. To assess the relative magnitude of variability over the two scan sessions, and to provide data to drive future sample size calculations, we

calculated the normalized Bland-Altman difference using the following equation:

$$D_{BA} = \frac{|\bar{D}_{12}|}{M} \times 100, \quad [4]$$

where \bar{D}_{12} is the average of the differences between scan 1 and scan 2 for the index of interest and M is the average value across both scans.

Finally, we employed an MAD analysis of repeated data. To fully utilize the data and to circumvent the instability of estimation based on bootstrap analyses with small sample sizes, we assumed that the indices derived from one eye are exchangeable and homogeneous, which is plausible for healthy subjects. This assumption allowed us to perform subject- and voxel-level resampling. In this case, the MAD was calculated from repeated data (for msh-DTI and ssh-DTI at $1.5 \times 1.5 \times 3 \text{ mm}^3$) rather than across eyes for one time point, and a lower MAD for a technique can be interpreted as a higher degree of reproducibility. Similarly, the $\Delta MAD\%$ is calculated and presented as the percent reduction in repeated-data variability of the msh-DTI compared with the ssh-DTI. Overlap of the 95% confidence interval for the MAD is a reason not to reject the null hypothesis ($\alpha = 0.05$) in that variations in the data derived from each time point are not different.

RESULTS

Figure 1 shows the impact of navigator-based motion correction on msh-DW and non-DW images acquired at $1.25 \times 3 \text{ mm}^3$ (in-plane \times slice thickness). The non-DW image with msh-DTI shows the optic nerves (Fig. 1a, arrows, dark core) clearly disambiguated from the CSF and largely free from artifacts. The DW msh-DTI image (Fig. 1b) shows that without correcting for motion-induced phase variations between shots, the optic nerves are not visible and significant ghosting can be appreciated. However, the DW image (Fig. 1c), which was obtained via 2D navigated motion correction, clearly shows both nerves (arrows).

Figures 2 and 3 compare ssh-DTI (Figs. 2a,b and 3a,b) and msh-DTI (Figs. 2c-f and 3c-f) images of the retrobulbar (Fig. 2) and intraorbital (Fig. 3) optic nerve for non-DW (Figs. 2a,c,e and 3a,c,e) and DW (Figs. 2b,d,f and 3b,d,f) acquisitions at $b = 500 \text{ s/mm}^2$ at $1.5 \times 3 \text{ mm}^3$

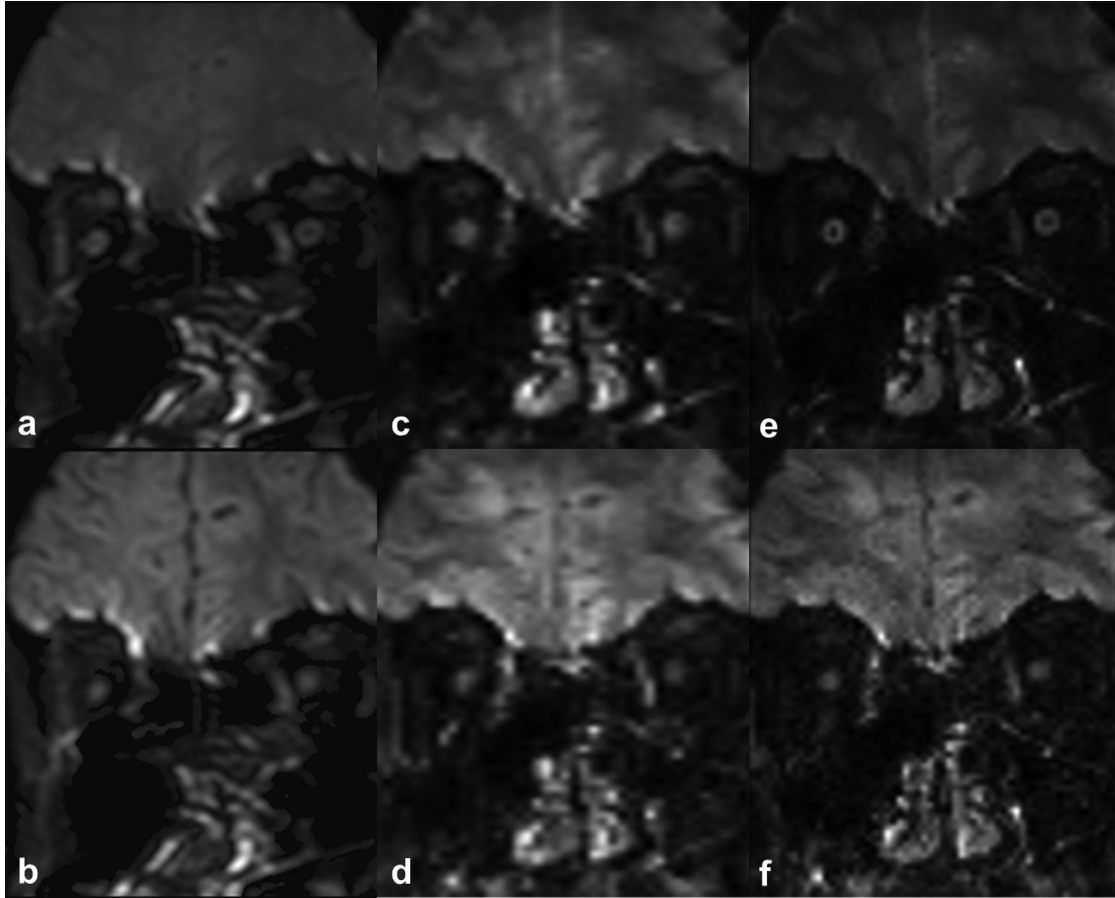


FIG. 2. Comparison between ssh-DTI (a,b) and msh-DTI (c–f) images for retrobulbar optic nerve regions for non-DW (a,c,e) and DW (b,d,f) acquisitions. The acquisition voxels were $1.5 \times 3 \text{ mm}^3$ (a–d) and $1.25 \times 3 \text{ mm}^3$ (e,f) for ssh-DTI (a,b) and msh-DTI (c–f) acquisitions.

(Figs. 2a–d and 3 a–d) and $1.25 \times 3 \text{ mm}^3$ (Figs. 2e,f and 3e,f) resolution. The size differences between optic nerve segments can be appreciated between different resolutions, and the conspicuity of the optic nerve is visibly greater in msh-DTI acquisitions than the ssh for both the $b = 500 \text{ s/mm}^2$ and the non-DW acquisitions. Also, little geometric distortion and blurring is appreciated in the msh DW (Figs. 2d,f and 3d,f) and non-DW (Figs. 2c,e and 3c,e) scans near the ocular muscles and inferior brain tissue. Note that larger partial volume effects are seen in msh with 1.5 mm^2 versus 1.25 mm^2 , but geometric distortions are substantially smaller compared with single-shot counterparts.

Figure 4 presents DTI-derived maps (FA, MD, λ_{\parallel} , and λ_{\perp}) from ssh-DTI and msh-DTI ($1.25 \times 2 \text{ mm}^3$) for both optic nerves. The ssh-DTI maps show significant geometric distortions and blurring in both nerves and signal asymmetry across nerves, whereas the msh-DTI results show consistent bilateral nerve morphology and better contrast between the nerve and CSF than their ssh-DTI counterparts. Both optic nerves are clearly delineated in all msh-DTI-derived maps and show lower MD, λ_{\parallel} , and λ_{\perp} values and higher FA values compared with surrounding CSF. In the msh FA map, the right optic nerve is a bright isolated spot, whereas the left optic nerve is less clear. In the ssh images, the right optic nerve is poorly resolved due to distortions, blurring, and partial

voluming with CSF, whereas the left optic nerve shows relatively clear FA and MD contrast and smaller image distortions. In general, the ssh-DTI maps show poorer or similar contrasts in all DTI-derived maps compared with the msh-DTI maps.

Quantitative DTI-Derived Indices

Table 2 presents the descriptive and inferential statistics of the DTI-derived indices across acquisition methods and voxel sizes for each eye. When comparing ssh-DTI and msh-DTI indices at $1.5 \times 3 \text{ mm}^3$ resolution, the average (over right and left) FA was lower and the diffusivities were higher in msh-DTI indices. However, for exclusively msh-DTI, at increasing resolution, the FA increased while the diffusivities decreased, potentially from reduced partial volume effects.

Because we studied only healthy subjects, we did not expect an appreciable asymmetry between optic nerves. However, for ssh acquisition, all DTI-derived indices were significantly different between the left and right optic nerves (weighted t test; FA, $P < 0.001$; MD, $P = 0.002$; λ_{\perp} , $P = 0.003$; λ_{\parallel} , $P = 0.004$). For msh-DTI, small differences were noted between the right and left optic nerves, even over different voxel sizes ($1.5 \times 1.5 \times 3 \text{ mm}^3$, $P = 0.3\text{--}0.4$; $1.25 \times 1.25 \times 3 \text{ mm}^3$, $P = 0.07\text{--}0.6$; $1.25 \times 1.25 \times 2 \text{ mm}^3$, $P = 0.02\text{--}0.2$) with the only significant difference being MD at $1.25 \times 1.25 \times 2 \text{ mm}^3$ ($P = 0.02$).

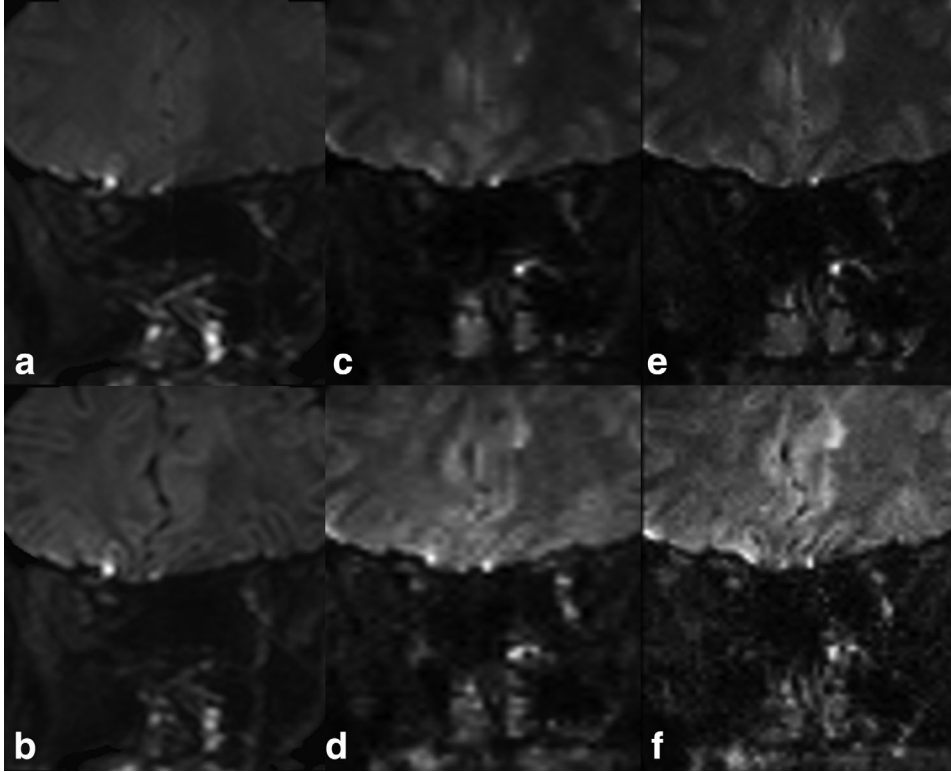


FIG. 3. Comparison between ssh-DTI (a,b) and msh-DTI (c-f) images for intraorbital optic nerve regions for non-DW (a,c,e) and DW (b,d,f) acquisitions. The acquisition voxels were $1.5 \times 3 \text{ mm}^3$ (a-d) and $1.25 \times 3 \text{ mm}^3$ (e,f) for ssh-DTI (a,b) and msh-DTI (c-f) acquisitions.

We also compared the impact of resolution on the mean values of the msh-DTI-derived indices. All DTI-derived indices were statistically different (at $\alpha = 0.05$) between in-plane resolutions of 1.5 mm^2 and 1.25 mm^2 (FA, $P < 0.001$; MD, $P < 0.001$; λ_{\perp} , $P < 0.001$; λ_{\parallel} , $P = 0.03$), yet no significant differences were observed between msh-DTI acquisitions with 2 and 3 mm slice thickness for in-plane resolution = 1.25 mm. This suggests that higher in-plane resolution decreases the impact of partial volume with surrounding CSF regions more so than slice thickness.

We next compared ssh-DTI with msh-DTI acquisitions at matched resolutions in two ways. First, we examined the weighted means of each index over both eyes. At $1.5 \times 1.5 \times 3 \text{ mm}^3$, all DTI-derived indices depended significantly on technique (between ssh and msh; FA, $P = 0.02$; MD, $P < 0.001$; λ_{\perp} , $P < 0.001$; λ_{\parallel} , $P < 0.001$). We hypothesize that this is likely due to blurring, geometric distortion, and variation across eyes seen in the ssh method and indicates that the descriptive statistics may be dependent on optic nerve orientation in the ssh case (see Discussion). A source of error can arise from nested variance, and the use of a weighted mean may overestimate the impact of technique. Therefore, we also compared resolution-matched ssh-DTI-derived and msh-DTI-derived indices using the MAD statistical framework. Briefly, we report the MAD (mean absolute difference between the right and left optic nerves drawn from an empirically determined distribution), the 95% CI for MAD, and the $\Delta\text{MAD}\%$, which is the relative difference between the ssh-DTI and msh-DTI MAD value (note that a negative value indicates improved MAD in the msh-DTI case compared to the ssh). Table 3 shows that MAD

analysis ($\alpha = 0.05$) revealed no statistical evidence that the disparity between the right and left optic nerves is significant. One could loosely claim that there is no difference in the mean values of the two methods to draw an analogy to analysis of variance. However, the fact that the MAD was reduced in the msh-DTI acquisition compared with the ssh-DTI acquisition suggests an improvement in the $\Delta\text{MAD}\%$ of about 3% (λ_{\perp}) to 17% (FA), indicating that across eyes, msh-DTI outperforms ssh-DTI.

Reproducibility

In addition to comparison of indices across resolutions, we considered the reproducibility of the technique over time and an estimate of the robustness to voxel placement. The latter is critical for understanding the impact that such a technique can have in the clinic when manual ROIs are drawn for every patient/time. We compared each method across two time points using Bland-Altman and Wilcoxon signed-rank tests for each acquisition and resolution (Table 4). The absolute mean differences ($|\bar{D}_{12}|$) of the indices between two visits (scan 1 and scan 2 in Table 4) were all small; additionally, Wilcoxon signed-rank tests demonstrated no statistically significant differences in the index mean values across visits for all acquisitions. Comparing msh-DTI $1.25 \times 2 \text{ mm}^3$ with the ssh-DTI $1.5 \times 3 \text{ mm}^3$ acquisitions, each msh DTI-derived index had a lower D_{BA} compared with ssh-DTI. For each $1.25 \times 2 \text{ mm}^3$, the D_{BA} remained below 10%, indicating a high degree of reliability. However, the msh-DTI acquisition with $1.5 \times 3 \text{ mm}^3$ and $1.25 \times 3 \text{ mm}^3$ voxels showed larger D_{BA} than ssh-DTI for FA ($1.5 \times 3 \text{ mm}^3$) and λ_{\perp} ($1.25 \times 3 \text{ mm}^3$).

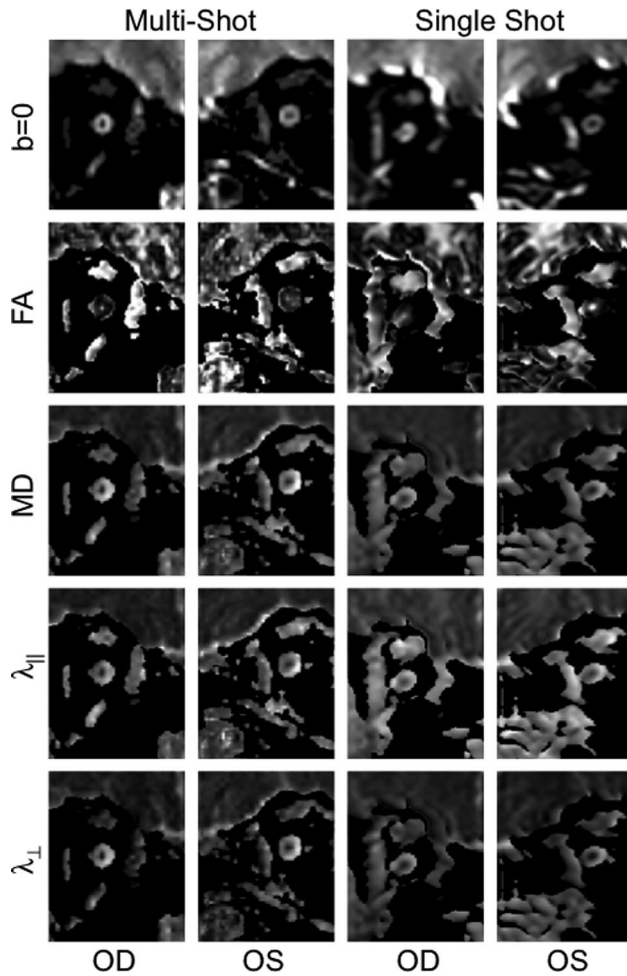


FIG. 4. Maps of FA, MD, $\lambda_{||}$, and λ_{\perp} for the right and left optic nerves from each of representative msh-DTI (left two columns) and ssh-DTI (right two columns) acquisitions with $1.25 \times 3 \text{ mm}^3$ and $1.5 \times 3 \text{ mm}^3$ voxels for msh-DTI and ssh-DTI, respectively.

When comparing msh and ssh at matched resolution, the msh D_{BA} was lower for all diffusivities (except FA) coarsely indicating a smaller variability across acquisitions when using msh-DTI acquisitions. However, as with cross-sectional analyses, we may have overestimated the differences due to nested variance and thus assessed MAD analyses between time points for matched resolutions as described in the Methods. In this case, the MAD is the difference between time 1 and time 2 for either optic nerve, as they are assumed to be interchangeable (see Methods). Table 5 shows that in all derived indices except $\lambda_{||}$, msh-MAD was lower than ssh-

MAD, but there was no statistical evidence at the $\alpha = 0.05$ level that the reproducibility was significantly different between the two techniques. It should be noted, however, that the $\Delta MAD\%$ was improved (negative $\Delta MAD\%$) in msh-DTI compared with ssh-DTI ($\sim 30\%$ – 40% decrease) for indices except msh $\lambda_{||}$, which performs approximately 10% more poorly than ssh-DTI. To summarize the data presented in Table 2 and Table 4, Figure 5 presents box plots comparing diffusion indices for right and left optic nerve asymmetry (Fig. 5a) and test-retest reproducibility (Fig. 5b) for each diffusion index. It should be pointed out, that the box plot demonstrates the median, intraquartile range and outliers of each index rather than the weighted mean over slices. It is important to present the box plot data in this manner to demonstrate the impact of comparing the weighted contributions of each person on the summary statistics.

DISCUSSION

We implemented a DW msh-EPI with SENSE and 2D-navigated motion correction to study the human optic nerve in vivo. DTI-derived indices of FA, MD, $\lambda_{||}$, and λ_{\perp} were acquired and compared between conventional ssh-DTI and msh-DTI approaches. When visually compared at the same resolution, msh-DTI provides much less geometric distortions and blurring effects compared with conventional ssh-EPI approaches. The descriptive statistics indicate that DTI-derived indices are consistent with previous reports of healthy subjects. For example, Chabert et al. (8) reported FA values of 0.39–0.56 and MD values of 0.8–1.3 $\mu\text{m}^2/\text{ms}$, and Wheeler-Kingshott et al. (20) reported FA values of 0.57–0.64 and MD values of 1.17–1.27 $\mu\text{m}^2/\text{ms}$ whereas our study revealed an FA range of 0.51–0.64 and an MD range of 0.87–1.44 $\mu\text{m}^2/\text{ms}$ [see Figure 6 in Techavipoo et al. (17) for values reported for other studies]. Interestingly, asymmetry between left and right optic nerves are not significant in Techavipoo et al. (17) even before the correction of susceptibility-induced distortions using field mapping, though the values from the right optic nerve tended to be lower than those for the left optic nerve. This can be attributed to ocular fixation during scanning, larger number (32 versus 15) of diffusion-encoding directions, and CSF suppression. Although we chose less-constrained imaging conditions for our subjects in anticipation of clinical implementation and comparison across techniques, assessing the impact of adapting such techniques for msh and ssh techniques is necessary. The main benefit, however, is the ability to improve optic nerve DTI by reducing EPI artifacts for optic nerve DW imaging at higher resolution. Because the msh-DTI methods are

Table 2
Mean \pm Standard Deviation of Diffusion Indices for Right and Left Optic Nerves

Method	Voxel size (mm^3)	FA		MD ^a		$\lambda_{ }$ ^a		λ_{\perp} ^a	
		Right	Left	Right	Left	Right	Left	Right	Left
ssh	$1.5 \times 1.5 \times 3$	0.52 ± 0.13	0.62 ± 0.15	1.09 ± 0.32	0.87 ± 0.37	1.74 ± 0.43	1.48 ± 0.45	0.76 ± 0.3	0.56 ± 0.35
msh	$1.5 \times 1.5 \times 3$	0.54 ± 0.11	0.51 ± 0.11	1.35 ± 0.42	1.44 ± 0.39	2.17 ± 0.58	2.28 ± 0.54	0.94 ± 0.37	1.03 ± 0.36
	$1.25 \times 1.25 \times 3$	0.63 ± 0.13	0.59 ± 0.13	1.14 ± 0.48	1.22 ± 0.47	1.99 ± 0.73	2.06 ± 0.7	0.73 ± 0.41	0.81 ± 0.42
	$1.25 \times 1.25 \times 2$	0.64 ± 0.13	0.62 ± 0.15	1.11 ± 0.44	1.27 ± 0.44	1.96 ± 0.65	2.17 ± 0.64	0.69 ± 0.37	0.82 ± 0.4

^aScale: $\mu\text{m}^2/\text{ms}$.

Table 3
MAD Between Left and Right Optic Nerves at the Initial Time Point and 95% CI (MAD) and Relative Improvement (–) or Worsening (+) of msh-DTI Versus ssh-DTI

Method	Voxel size (mm ³)	FA			MD ($\mu\text{m}^2/\text{ms}$)			λ_{\parallel} ($\mu\text{m}^2/\text{ms}$)			λ_{\perp} ($\mu\text{m}^2/\text{ms}$)		
		MAD	95% CI	$\Delta\text{MAD}\%$	MAD ($\times 10^{-1}$)	95% CI ($\times 10^{-1}$)	$\Delta\text{MAD}\%$	MAD ($\times 10^{-1}$)	95% CI ($\times 10^{-1}$)	$\Delta\text{MAD}\%$	MAD ($\times 10^{-1}$)	95% CI ($\times 10^{-1}$)	$\Delta\text{MAD}\%$
ssh	$1.5 \times 1.5 \times 3$	0.18	(0.15, 0.2)	–16.7	4.2	(3.5, 5.1)	–14.3	5.4	(4.0, 6.6)	–13.0	3.9	(3.3, 4.4)	–2.6
msh	$1.5 \times 1.5 \times 3$	0.15	(0.13, 0.17)		3.6	(3.1, 4.0)		4.7	(4.1, 5.2)		3.8	(3.2, 4.3)	

limited by time and not echo-train length, it is conceivable to extend this approach to 1 mm or less in-plane resolution with little impact from EPI-related artifacts.

All DTI-derived indices were significantly asymmetric in ssh-DTI scans, but not in the msh-DTI comparisons across eyes. This suggests that msh-DTI acquisitions may be more robust than ssh-DTI for bilateral comparisons of optic nerves and more reliable for unilateral acquisitions. Additionally, we showed that the test–retest reproducibility was not significantly different across time points for all acquisitions, which agrees with previous ssh-DTI literature. Although msh-DTI acquisitions resulted in generally lower D_{BA} than ssh-DTI acquisitions, we observed minor exceptions in msh-DTI. This is not surprising due to the greater sensitivity of msh-DTI methods (i.e., a blurry image is often more reproducible than a sharp image due to the sensitivity to borders and ROI placement). It is somewhat inappropriate to compare the reproducibility of ssh-DTI with msh-DTI at different resolutions due to the impact of SNR, contrast-to-noise ratio (CNR), and general blurring in ssh-DTI acquisitions. When considering matched resolution, there is an approximately 30% reduction in the scan-to-scan variability in msh-DTI compared with ssh-DTI. Visually, msh-DTI acquisitions showed superior image quality and optic nerve conspicuity when compared with ssh-DTI. It should be noted that low CNR and poor resolution may lead to greater scan–rescan reliability, and future statistical studies could derive statistical models that penalize scans with poor resolution and/or CNR.

We chose to compare scans with an equal scan time unit rather than adjusting angular resolution of diffusion gradients that can adversely impact the fidelity of the derived indices (49). Therefore, ssh-DTI scans were acquired with more signal acquisitions (N_{avg}) than the msh-DTI scans to match the scan time, e.g., $N_{\text{avg}} = 10$ ($1.5 \times 3 \text{ mm}^3$) for ssh-DTI versus $N_{\text{avg}} = 8$ ($1.5 \times 3 \text{ mm}^3$) and $N_{\text{avg}} = 5$ (1.25 mm^2) for msh-DTI. Although increasing N_{avg} can increase SNR, EPI-related artifacts cannot be reduced unless the EPI echo-train length is reduced. With the developed acquisition and reconstruction methods, DTI scans have been performed with higher phase-encoding bandwidth (ssh = 34 Hz versus msh = 91 Hz) and shorter echo-trains [52 in Kim et al. (12) and 48 in Xu et al. (21)] compared with conventional ssh-DTI; consequently, clearer optic nerve images can be appreciated and image distortion, blurring, and eddy current effects can be mitigated significantly.

The msh-DTI imaging sequence only acquires a segment of k -space for each excitation, and k -space is filled over multiple TR periods. When the diffusion gradients are on, gross subject or physiological motions can generate an additional phase in the DW signal, proportional to the magnitude of motion or the gradient. The phase variation depends on the orientations of the axis of rotation and the applied diffusion gradient. Therefore, more than a one-dimensional navigator is required for correction of motion-induced phase errors typical in msh-DTI acquisitions. In this study, a 2D navigator-echo was acquired using additional EPI readout for more accurate corrections of in-plane phase variations. The use of 2D navigators for phase correction has been effective even for the

Table 4
Reproducibility Results from Bland-Altman and Wilcoxon Signed-Rank Test

Method	Voxel size (mm ³)	Scans (mean \pm SD)		\bar{D}_{12}^{\dagger}	95% CI (D) ^a	Limit of agreement ^a	P^b	D _{BA} (%)
		Scan 1	Scan 2					
FA								
ssh	1.5 \times 1.5 \times 3	0.52 \pm 0.08	0.54 \pm 0.07	−0.03	(−0.17, 0.12)	(−0.26, 0.20)	0.81	5.49
msh	1.5 \times 1.5 \times 3	0.54 \pm 0.07	0.47 \pm 0.13	0.08	(−0.03, 0.19)	(−0.10, 0.26)	0.13	15.65
	1.25 \times 1.25 \times 3	0.59 \pm 0.09	0.61 \pm 0.05	−0.02	(−0.13, 0.08)	(−0.22, 0.18)	0.69	3.55
	1.25 \times 1.25 \times 2	0.62 \pm 0.05	0.62 \pm 0.05	0.01	(−0.08, 0.06)	(−0.14, 0.12)	0.81	1.21
MD ^a								
ssh	1.5 \times 1.5 \times 3	1.20 \pm 0.26	1.0 \pm 0.23	0.21	(−0.25, 0.66)	(−0.52, 0.94)	0.31	18.94
msh	1.5 \times 1.5 \times 3	1.53 \pm 0.43	1.51 \pm 0.37	0.02	(−0.38, 0.42)	(−0.62, 0.66)	0.88	1.41
	1.25 \times 1.25 \times 3	1.53 \pm 0.42	1.26 \pm 0.31	0.27	(−0.07, 0.61)	(−0.39, 0.93)	0.09	19.15
	1.25 \times 1.25 \times 2	1.31 \pm 0.32	1.41 \pm 0.34	−0.09	(−0.39, 0.20)	(−0.67, 0.48)	0.44	6.98
λ_{\parallel}^a								
ssh	1.5 \times 1.5 \times 3	1.9 \pm 0.41	1.60 \pm 0.32	0.31	(−0.45, 1.08)	(−0.92, 1.54)	0.44	17.87
msh	1.5 \times 1.5 \times 3	2.51 \pm 0.59	2.38 \pm 0.61	0.12	(−0.51, 0.75)	(−0.89, 1.14)	0.63	5.03
	1.25 \times 1.25 \times 3	2.5 \pm 0.55	2.15 \pm 0.52	0.36	(−0.23, 0.94)	(−0.77, 1.49)	0.16	15.47
	1.25 \times 1.25 \times 2	2.23 \pm 0.42	2.39 \pm 0.6	−0.16	(−0.67, 0.36)	(−1.15, 0.84)	0.56	6.77
λ_{\perp}^a								
ssh	1.5 \times 1.5 \times 3	0.85 \pm 0.22	0.7 \pm 0.19	0.16	(−0.17, 0.49)	(−0.37, 0.69)	0.44	20.15
msh	1.5 \times 1.5 \times 3	1.05 \pm 0.36	1.07 \pm 0.28	−0.03	(−0.51, 0.75)	(−0.50, 0.44)	0.88	2.71
	1.25 \times 1.25 \times 3	1.04 \pm 0.38	0.82 \pm 0.21	0.21	(−0.08, 0.51)	(−0.35, 0.78)	0.06	22.91
	1.25 \times 1.25 \times 2	0.85 \pm 0.27	0.92 \pm 0.22	−0.06	(−0.27, 0.14)	(−0.45, 0.32)	0.56	7.25

^aScale: $\mu\text{m}^2/\text{ms}$.

^bWilcoxon signed-rank test.

correction of nonlinear motion-induced phases (e.g., nonlinear brain motion by cardiac pulsation) (36).

A major difficulty in optic nerve imaging is rapid, random eye motion, which affects the position/orientation of the optic nerve. Although ssh-DTI can acquire an image within a fraction of a second, there is still the effect between acquisitions for different diffusion gradient orientations and averaging, and probable image degradation when half Fourier acquisition is used (50). Although the optic nerve is visually more conspicuous in msh non-DW and DW images than in ssh-DTI images (Figs. 2 and 3), larger, uncompensated motion effects hamper msh-DTI more so than ssh-DTI. Previous literature shows that averaging a large number of acquisitions (>40) can reduce the effect of motion and is effective for localization of the

optic nerve when the ZOOM technique is used (10,19,20). In the current study, five to eight acquisitions were averaged for msh-DTI scans (10 for ssh-DTI) to cover 12 slices (36 mm with 3 mm slice thickness) with 15 DW gradients. These scan parameters provided high-quality msh non-DW and DW images within a clinically acceptable scan time (<8 min) with reduced Nyquist violation in msh scans [≥ 4 acquisitions for averaging (51)], extended coverage along the optic nerve [36 mm (42)], and reduced variation in DTI-derived indices [≥ 6 directions (52)]. Although the scan time constraint in the presence of other scan parameters allowed relatively short msh TRs (~ 2 s), there was no significant visual impact on msh non-DW and DW images (Figs. [1 and 2], and 3) or derived indices (Fig. 4). The left optic nerve appeared

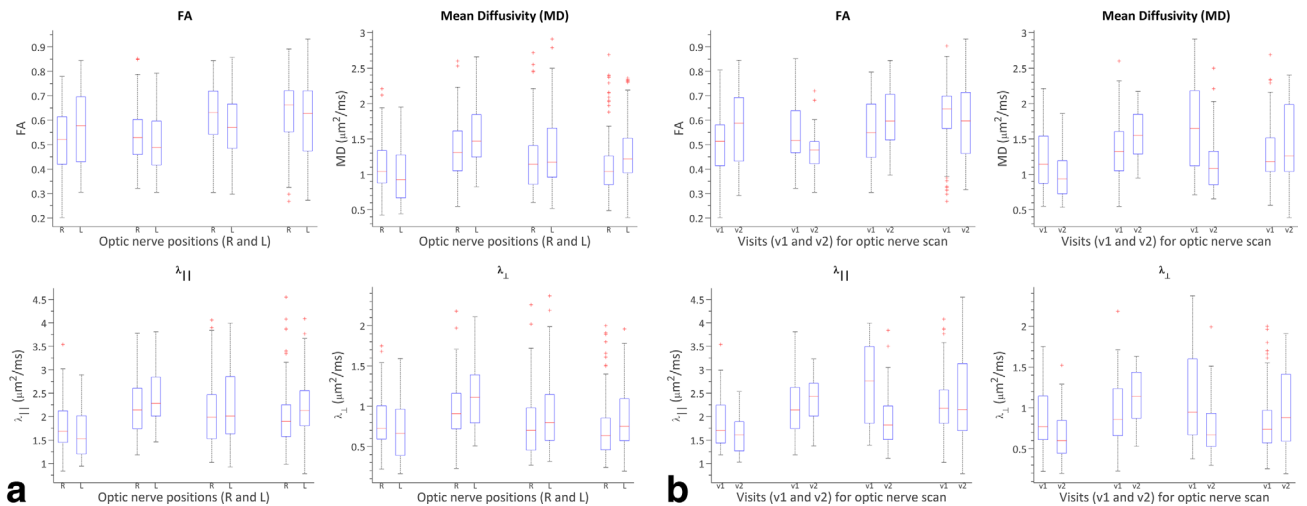


FIG. 5. Box plots comparing diffusion indices for right (R) and left (L) optic nerve asymmetry (a) and test (v1) and retest (v2) reproducibility (b) for each of diffusion indices.

Table 5
MAD Between Initial and Follow-up Examination and 95% CI (MAD) and Relative Improvement (–) or Worsening (+) of msh-DTI Versus ssh-DTI

Method	Voxel size (mm ³)	FA				λ_{\parallel} ($\mu\text{m}^2/\text{ms}$)				λ_{\perp} ($\mu\text{m}^2/\text{ms}$)			
		MAD	95% CI	$\Delta\text{MAD}\%$	MAD ($\times 10^{-1}$)	95% CI ($\times 10^{-1}$)	$\Delta\text{MAD}\%$	MAD ($\times 10^{-1}$)	95% CI ($\times 10^{-1}$)	$\Delta\text{MAD}\%$	MAD ($\times 10^{-1}$)	95% CI ($\times 10^{-1}$)	$\Delta\text{MAD}\%$
ssh	$1.5 \times 1.5 \times 3$	0.21	(0.15, 0.32)	–28.6	5.1	(2.8, 8.1)	–31.4	5.1	(3.1, 6.9)	9.8	5.3	(3.0, 9.0)	–37.7
msh	$1.5 \times 1.5 \times 3$	0.15	(0.11, 0.17)		3.5	(2.0, 5.1)		5.6	(3.9, 6.9)		3.3	(3.2, 4.6)	

Data were selected from a distribution that contained only the right eye but were assumed to be exchangeable and homogeneous.

less clearly than the right optic nerve in the msh-DTI FA map, which may be due to eye motion and/or a partial volume effect from posteromedially running optic nerve geometry; this is because the effect was manifested in the left optic nerve diffusivity maps, where the nasal-lateral aspect of the left optic nerve region appeared darker than the medial aspect.

It should be noted that this study was designed to image both optic nerves simultaneously for comparisons with conventional acquisition methodology. The optic nerve does not follow a straight path, and in most subjects the intraorbital optic nerve courses oblique to the imaging plane. In addition, uncontrolled eye movement without ocular fixation and uncompensated CSF signal may affect DTI measurements as well as major white matter tracts (53,54), depending on the amount of eye motion, nerve angulations, and slice thicknesses. The results suggest that increased through-plane partial volume effects are more detrimental in tissue–CSF than tissue–tissue boundaries. One potential way to mitigate through-plane partial volume would be to study each optic nerve individually and set the imaging planes as coronal (or sagittal/axial) to each nerve or perform CSF suppression. Also notable is the reduction of water signal intensity by radiofrequency pulses (SPAIR or spectrally selective attenuated inversion recovery [SPAIR]) or gradient inversion. This unwanted suppression of water signals, in particular, can cause extra signal loss resulting in errors in quantitative DTI analysis. Future studies could include a study of appropriate tissue and CSF suppression techniques for msh-DTI.

The entire cohort in this study was made up of healthy subjects. The next step is to evaluate whether msh-DTI can provide a viable alternative to ssh-DTI for studies of optic nerve pathologies. We suspect higher resolution would be necessary in such cases, which is feasible with msh-DTI. Finally, purpose-designed and higher-channel receive coils could improve upon the optic nerve methodology presented here with a conventional eight-channel SENSE head coil.

ACKNOWLEDGMENTS

We thank Donna Butler, Leslie McIntosh, Kristen George-Durrett, and David Pennell for their expert MRI assistance. We also appreciate the contributions by Philips Medical Systems, Charles Nockowski, and Ryan Robison.

REFERENCES

- Balcer LJ. Clinical practice. Optic neuritis. *New Engl J Med* 2006;354:1273–1280.
- Hickman SJ, Miszkil KA, Plant GT, Miller DH. The optic nerve sheath on MRI in acute optic neuritis. *Neuroradiology* 2005;47:51–55.
- Kupersmith MJ, Alban T, Zeiffer B, Lefton D. Contrast-enhanced MRI in acute optic neuritis: relationship to visual performance. *Brain* 2002;125:812–822.
- Boorstein JM, Moonis G, Boorstein SM, Patel YP, Culler AS. Optic neuritis: imaging with magnetization transfer. *AJR Am J Roentgenol* 1997;169:1709–1712.
- Dousset V, Grossman RI, Ramer KN, Schnall MD, Young LH, Gonzalez-Scarano F, Lavi E, Cohen JA. Experimental allergic encephalomyelitis and multiple sclerosis: lesion characterization with magnetization transfer imaging. *Radiology* 1992;182:483–491.
- Hickman SJ, Toosy AT, Jones SJ, Altmann DR, Miszkil KA, MacManus DG, Barker GJ, Plant GT, Thompson AJ, Miller DH. Serial

- magnetization transfer imaging in acute optic neuritis. *Brain* 2004; 127:692–700.
7. Schmierer K, Scaravilli F, Altmann DR, Barker GJ, Miller DH. Magnetization transfer ratio and myelin in postmortem multiple sclerosis brain. *Ann Neurol* 2004;56:407–415.
8. Chabert S, Molko N, Cointepas Y, Le Roux P, Le Bihan D. Diffusion tensor imaging of the human optic nerve using a non-CPMG fast spin echo sequence. *J Magn Reson Imaging* 2005;22:307–310.
9. Dowell NG, Jenkins TM, Ciccarelli O, Miller DH, Wheeler-Kingshott CA. Contiguous-slice zonally oblique multislice (CO-ZOOM) diffusion tensor imaging: examples of in vivo spinal cord and optic nerve applications. *J Magn Reson Imaging* 2009;29:454–460.
10. Hickman SJ, Wheeler-Kingshott CA, Jones SJ, Mischkiel KA, Barker GJ, Plant GT, Miller DH. Optic nerve diffusion measurement from diffusion-weighted imaging in optic neuritis. *AJNR Am J Neuroradiol* 2005;26:951–956.
11. Iwasawa T, Matoba H, Ogi A, Kurihara H, Saito K, Yoshida T, Matsubara S, Nozaki A. Diffusion-weighted imaging of the human optic nerve: a new approach to evaluate optic neuritis in multiple sclerosis. *Magn Reson Med* 1997;38:484–491.
12. Kim SE, Jeong EK, Kim TH, Hadley JR, Minagla E, Anderson J, Parker DL. In Vivo Diffusion Tensor Imaging of Human Optic Nerve Using 2D Interleaved Inner Volume Technique on 3T System. In Proceedings of the 16th Annual Meeting of ISMRM, Toronto, Ontario, Canada, 2008. p. 1815.
13. Naismith RT, Xu J, Snyder A, Benzinger T, Shimony J, Trinkaus K, Cross AH, Song SK. Axial Diffusivity in Acute and Isolated Optic Neuritis. In Proceedings of the 16th Annual Meeting of ISMRM, Toronto, Ontario, Canada, 2008. p. 3392.
14. Naismith RT, Xu J, Tutlam NT, Snyder A, Benzinger T, Shimony J, Shepherd J, Trinkaus K, Cross AH, Song SK. Disability in optic neuritis correlates with diffusion tensor-derived directional diffusivities. *Neurology* 2009;72:589–594.
15. Smith SA, Williams ZR, Ratchford JN, et al. Diffusion tensor imaging of the optic nerve in multiple sclerosis: association with retinal damage and visual disability. *AJNR Am J Neuroradiol* 2011;32:1662–1668.
16. Sun HH, Wang D, Zhang QJ, Bai ZL, He P. Magnetic resonance diffusion tensor imaging of optic nerve and optic radiation in healthy adults at 3T. *Int J Ophthalmol* 2013;6:868–872.
17. Techavipoo U, Okai AF, Lackey J, Shi J, Dresner MA, Leist TP, Lai S. Toward a practical protocol for human optic nerve DTI with EPI geometric distortion correction. *J Magn Reson Imaging* 2009;30:699–707.
18. van der Walt A, Kolbe SC, Wang YE, et al. Optic nerve diffusion tensor imaging after acute optic neuritis predicts axonal and visual outcomes. *PLoS One* 2013;8:e83825.
19. Wheeler-Kingshott CA, Parker GJ, Symms MR, Hickman SJ, Tofts PS, Miller DH, Barker GJ. ADC mapping of the human optic nerve: increased resolution, coverage, and reliability with CSF-suppressed ZOOM-EPI. *Magn Reson Med* 2002;47:24–31.
20. Wheeler-Kingshott CA, Trip SA, Symms MR, Parker GJ, Barker GJ, Miller DH. In vivo diffusion tensor imaging of the human optic nerve: pilot study in normal controls. *Magn Reson Med* 2006;56:446–451.
21. Xu JG, Naismith RT, Trinkaus KM, Cross AH, Song SK. Towards Accurate In Vivo Diffusion Measurement in Human Optic Nerve. In Proceedings of the 15th Annual Meeting of ISMRM, Berlin, Germany, 2007. p. 11.
22. Basser PJ, Mattiello J, LeBihan D. Estimation of the effective self-diffusion tensor from the NMR spin echo. *J Magn Reson B* 1994;103:247–254.
23. Moseley ME, Cohen Y, Kucharczyk J, Mintorovitch J, Asgari HS, Wendland MF, Tsuruda J, Norman D. Diffusion-weighted MR imaging of anisotropic water diffusion in cat central nervous system. *Radiology* 1990;176:439–445.
24. Basser PJ, Pierpaoli C. Microstructural and physiological features of tissues elucidated by quantitative-diffusion-tensor MRI. *J Magn Reson B* 1996;111:209–219.
25. Le Bihan D, Breton E, Lallemand D, Grenier P, Cabanis E, Laval-Jeantet M. MR imaging of intravoxel incoherent motions: application to diffusion and perfusion in neurologic disorders. *Radiology* 1986;161:401–407.
26. Trip SA, Wheeler-Kingshott C, Jones SJ, Li WY, Barker GJ, Thompson AJ, Plant GT, Miller DH. Optic nerve diffusion tensor imaging in optic neuritis. *Neuroimage* 2006;30:498–505.
27. Frohman EM, Fujimoto JG, Frohman TC, Calabresi PA, Cutter G, Balcer LJ. Optical coherence tomography: a window into the mechanisms of multiple sclerosis. *Nat Clin Pract Neurol* 2008;4:664–675.
28. Turner R, Le Bihan D. Single-shot diffusion imaging at 2.0 Tesla. *J Magn Reson* 1990;86:445–452.
29. Pruessmann KP, Weiger M, Scheidegger MB, Boesiger P. SENSE: sensitivity encoding for fast MRI. *Magn Reson Med* 1999;42:952–962.
30. Anderson AW, Gore JC. Analysis and correction of motion artifacts in diffusion weighted imaging. *Magn Reson Med* 1994;32:379–387.
31. Ordidge RJ, Helpert JA, Qing ZX, Knight RA, Nagesh V. Correction of motional artifacts in diffusion-weighted MR images using navigator echoes. *Magn Reson Imaging* 1994;12:455–460.
32. Atkinson D, Counsell S, Hajnal JV, Batchelor PG, Hill DL, Larkman DJ. Nonlinear phase correction of navigated multi-coil diffusion images. *Magn Reson Med* 2006;56:1135–1139.
33. Butts K, Pauly J, de Crespigny A, Moseley M. Isotropic diffusion-weighted and spiral-navigated interleaved EPI for routine imaging of acute stroke. *Magn Reson Med* 1997;38:741–749.
34. Liu C, Bammer R, Kim DH, Moseley ME. Self-navigated interleaved spiral (SNAILS): application to high-resolution diffusion tensor imaging. *Magn Reson Med* 2004;52:1388–1396.
35. Liu C, Moseley ME, Bammer R. Simultaneous phase correction and SENSE reconstruction for navigated multi-shot DWI with non-cartesian k-space sampling. *Magn Reson Med* 2005;54:1412–1422.
36. Miller KL, Pauly JM. Nonlinear phase correction for navigated diffusion imaging. *Magn Reson Med* 2003;50:343–353.
37. Pipe JG, Farthing VG, Forbes KP. Multishot diffusion-weighted FSE using PROPELLER MRI. *Magn Reson Med* 2002;47:42–52.
38. Porter DA, Heidemann RM. High resolution diffusion-weighted imaging using readout-segmented echo-planar imaging, parallel imaging and a two-dimensional navigator-based reacquisition. *Magn Reson Med* 2009;62:468–475.
39. Frank LR, Jung Y, Inati S, Tyszka JM, Wong EC. High efficiency, low distortion 3D diffusion tensor imaging with variable density spiral fast spin echoes (3D DW VDS RARE). *Neuroimage* 2010;49:1510–1523.
40. Van AT, Hernando D, Sutton BP. Motion-induced phase error estimation and correction in 3D diffusion tensor imaging. *IEEE transactions on medical imaging* 2011;30:1933–1940.
41. Jeong HK, Gore JC, Anderson AW. High-resolution human diffusion tensor imaging using 2-D navigated multishot SENSE EPI at 7 T. *Magn Reson Med* 2013;69:793–802.
42. Barker GJ. Diffusion-weighted imaging of the spinal cord and optic nerve. *J Neurol Sci* 2001;186(suppl 1):S45–S49.
43. Butts K, Riederer SJ, Ehman RL, Thompson RM, Jack CR. Interleaved echo planar imaging on a standard MRI system. *Magn Reson Med* 1994;31:67–72.
44. Feinberg DA, Oshio K. Phase errors in multi-shot echo planar imaging. *Magn Reson Med* 1994;32:535–539.
45. Basser PJ. Inferring microstructural features and the physiological state of tissues from diffusion-weighted images. *NMR Biomed* 1995;8:333–344.
46. McAuliffe MJ, Lalonde FM, McGarry D, Gandler W, Csaky K, Trus B. Medical Image Processing, Analysis and Visualization in Clinical Research. In Proceedings of the 14th IEEE Symposium on Computer-Based Medical Systems (CBMS 2001), Bethesda, Maryland, USA, 2001. p. 381–386.
47. Bland JM, Kerry SM. Statistics notes. Weighted comparison of means. *BMJ* 1998;316:129.
48. Bland JM, Altman DG. Measuring agreement in method comparison studies. *Stat Methods Med Res* 1999;8:135–160.
49. Landman BA, Farrell JA, Jones CK, Smith SA, Prince JL, Mori S. Effects of diffusion weighting schemes on the reproducibility of DTI-derived fractional anisotropy, mean diffusivity, and principal eigenvector measurements at 1.5T. *Neuroimage* 2007;36:1123–1138.
50. Storey P, Frigo FJ, Hinks RS, Mock BJ, Collick BD, Baker N, Marmurek J, Graham SJ. Partial k-space reconstruction in single-shot diffusion-weighted echo-planar imaging. *Magn Reson Med* 2007;57:614–619.
51. Atkinson D, Porter DA, Hill DL, Calamante F, Connelly A. Sampling and reconstruction effects due to motion in diffusion-weighted interleaved echo planar imaging. *Magn Reson Med* 2000;44:101–109.
52. Jones DK. The effect of gradient sampling schemes on measures derived from diffusion tensor MRI: a Monte Carlo study. *Magn Reson Med* 2004;51:807–815.
53. Bhagat YA, Beaulieu C. Diffusion anisotropy in subcortical white matter and cortical gray matter: changes with aging and the role of CSF-suppression. *J Magn Reson Imaging* 2004;20:216–227.
54. Papadakis NG, Martin KM, Mustafa MH, Wilkinson ID, Griffiths PD, Huang CL, Woodruff PW. Study of the effect of CSF suppression on white matter diffusion anisotropy mapping of healthy human brain. *Magn Reson Med* 2002;48:394–398.